



This is a repository copy of *Estimation of trabecular bone parameters in children from multisequence MRI using texture-based regression*.

White Rose Research Online URL for this paper:
<http://eprints.whiterose.ac.uk/101167/>

Version: Accepted Version

Article:

Lekadir, K., Hoogendoorn, C., Armitage, P. et al. (4 more authors) (2016) Estimation of trabecular bone parameters in children from multisequence MRI using texture-based regression. *Medical Physics*, 43 (6). 3071. ISSN 0094-2405

<https://doi.org/10.1118/1.4950713>

Reuse

Unless indicated otherwise, fulltext items are protected by copyright with all rights reserved. The copyright exception in section 29 of the Copyright, Designs and Patents Act 1988 allows the making of a single copy solely for the purpose of non-commercial research or private study within the limits of fair dealing. The publisher or other rights-holder may allow further reproduction and re-use of this version - refer to the White Rose Research Online record for this item. Where records identify the publisher as the copyright holder, users can verify any specific terms of use on the publisher's website.

Takedown

If you consider content in White Rose Research Online to be in breach of UK law, please notify us by emailing eprints@whiterose.ac.uk including the URL of the record and the reason for the withdrawal request.



eprints@whiterose.ac.uk
<https://eprints.whiterose.ac.uk/>

1 **Estimation of Trabecular Bone Parameters in Children from Multi-**
2 **Sequence MRI using Texture-Based Regression**

3 Karim Lekadir^{1,†}, Corné Hoogendoorn¹, Paul Armitage², Elspeth Whitby², David King⁴,
4 Paul Dimitri^{5,*}, and Alejandro F. Frangi^{6,*}

5 ¹ Center for Computational Imaging & Simulation Technologies in Biomedicine,
6 Universitat Pompeu Fabra, Barcelona, Spain

7 ² The Academic Unit of Radiology, ³ The Academic Unit of Reproductive and Developmental Medicine,

8 ⁴ The Academic Unit of Child Health, ⁵ The Mellanby Centre for Bone Research,

9 ⁶ Center for Computational Imaging & Simulation Technologies in Biomedicine,
10 The University of Sheffield, Sheffield, United Kingdom

11 † Corresponding author, * Both senior authors have contributed equally

12
13
14
15 **Corresponding author:**

16
17 Karim Lekadir

18 Universitat Pompeu Fabra

19 Department of Information & Communication Technologies

20 C/ Roc Boronat 122-140

21 08018 Barcelona, Spain

22
23 Phone: +34 935 421 350

24 E-mail: karim.lekadir@upf.edu

25

26

27 **ABSTRACT**

28 **Purpose:** This paper presents a statistical approach for the prediction of trabecular bone parameters
29 from low-resolution multi-sequence MRI in children, thus addressing the limitations of high-
30 resolution modalities such as HR-pQCT, including the significant exposure of young patients to radia-
31 tion and the limited applicability of such modalities to peripheral bones in vivo.

32 **Methods:** A statistical predictive model is constructed from a database of MRI and HR-pQCT da-
33 taset, to relate the low resolution MRI appearance in the cancellous bone to the trabecular parameters
34 extracted from the high-resolution images. The description of the MRI appearance is achieved be-
35 tween subjects by using a collection of feature descriptors, which describe the texture properties in-
36 side the cancellous bone, and which are invariant to the geometry and size of the trabecular areas. The
37 predictive model is built by fitting to the training data a nonlinear partial least square regression be-
38 tween the input MRI features and the output trabecular parameters.

39 **Results:** Detailed validation based on a sample of 96 datasets shows **correlations > 0.7** between the
40 trabecular parameters predicted from low-resolution multi-sequence MRI based on the proposed sta-
41 tistical model and the values extracted from high-resolution HRp-QCT.

42 **Conclusion:** The obtained results indicate the promise of the proposed predictive technique for the
43 estimation of trabecular parameters in children from multi-sequence MRI, thus reducing the need for
44 high-resolution radiation-based scans for a fragile population that is under development and growth.

45 **Keywords:** Prediction of trabecular parameters, HR-pQCT, skeletal MRI, texture descriptors, feature
46 selection, partial least squares regression.

47 I. INTRODUCTION

48 The study of skeletal growth and development is an important yet challenging research area within
49 musculoskeletal imaging¹⁻⁵. The assessment of bone-microarchitecture^{6,7}, in particular, can provide
50 significant insight into the changes that occur during skeletal development in relation to skeletal integ-
51 rity, as well as a clearer understanding about the factors underpinning bone fracture and disease in
52 children and adolescents⁸⁻¹⁰.

53 Essentially, bone micro-architecture consists of an ensemble of separated anisotropic trabeculae,
54 which react to the loadings and stresses that the bone is subjected to¹¹. For the assessment of these
55 trabeculae, important parameters or morphometric indices can be calculated, which are measures
56 characterizing the three-dimensional microstructure of the cancellous bone¹². Amongst these, tra-
57 becular thickness (Tb.Th) estimates the mean thickness of the trabeculae. Additionally, trabecular
58 spacing or separation (Tb.Sp) measures mean space between the trabeculae. Another important pa-
59 rameter is the trabecular number (Tb.N), which indicates the number of trabeculae per unit length
60 (mm)¹².

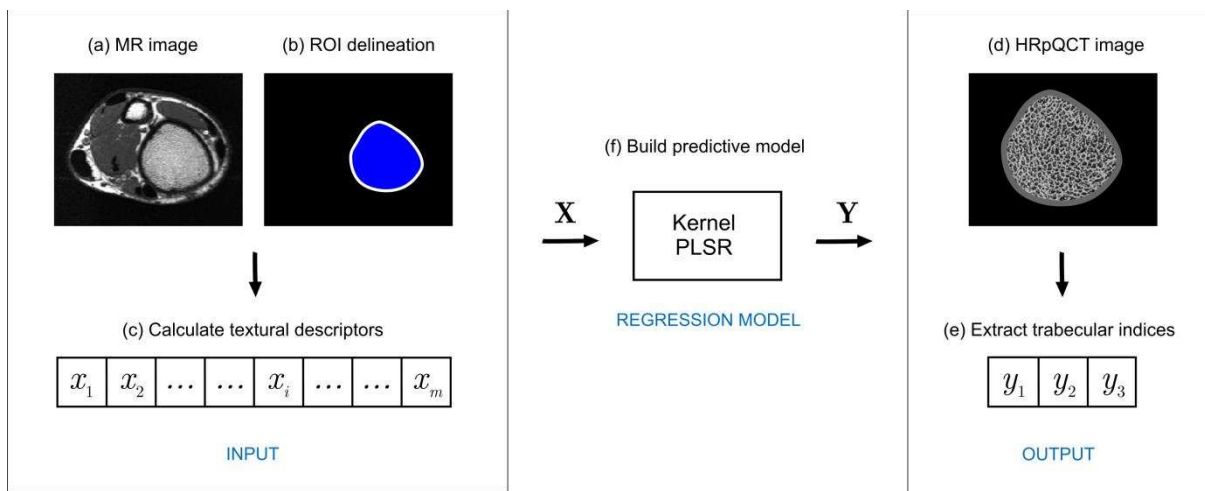
61 To estimate these parameters, imaging of the cancellous bone in very high detail is required, i.e.
62 through imaging modalities that can produce much higher image resolutions than those commonly
63 used in clinical practice such as standard magnetic resonance imaging (MRI). Two candidate modali-
64 ties for this purpose are micro-CT¹³ and high-resolution peripheral quantitative CT (HR-pQCT)¹⁴.
65 Micro-CT (isotropic resolution – 8 μ m) is only limited to ex vivo imaging following bone biopsy and
66 thus far has been used mostly for orthopedic research^{15,16}. On the other hand, while HR-pQCT (iso-
67 tropic voxel size 82 μ m) has shown promise for bone assessment in adolescents¹⁷, the modality can
68 only be used to acquire high-resolution images of the ultra-distal radius and tibia (9mm)^{14,17,18} and so
69 may not provide an accurate reflection of proximal appendicular and axial skeletal microstructure.
70 Furthermore, the radiation associated with X-ray based modalities limits their routine use in clinical
71 practice for children and adolescents, in particular in longitudinal studies that require repetition exam-
72 inations to assess bone strength/growth over time.

73 Amongst alternative imaging modalities, Magnetic Resonance Imaging (MRI) provides a potential
74 solution to bone imaging in children as it imparts no ionizing radiation. For example, high-resolution
75 images derived from 3T and 7T MRI scanners have been investigated as a means of assessing tra-
76 becular bone but it is limited to research studies as special coils and sequences analysis are required,
77 although there is clear potential for future clinical application^{19, 20}. Standard clinical 1.5 T MRI, on
78 the other hand, provides a unique image-weighting contrast mechanism by varying the acquisition
79 parameters to exploit tissue relaxation properties (e.g., T1 recovery, T2 decay), thus producing a mul-
80 ti-sequence stack for the same image. Each MRI sequence typically displays distinct appearance
81 properties, thus highlighting varying aspects of the tissue under investigation.

82 Cortical bone and trabecular bone have extremely short intrinsic T_2 (proton relaxation time) values
83 (0.4-0.5 milliseconds), low water content, and thus relatively low MR-detectable magnetization thus
84 producing a limited signal and appearing dark next to bone marrow (white) on conventional MRI
85 sequences. Water is predominantly bound to collagen with the remaining fraction found in micropores
86 of the Haversian and the lacunar-canalicular system of cortical bone. Conventional MRI sequences
87 use spin-echo imaging with relaxation times (TE's) of 8-10 milliseconds and with gradient echo pulse
88 reducing TEs to 1-2 milliseconds. Recently pulse sequences with even shorter TEs in the range of
89 0.05–0.20 milliseconds have been developed by the use of half radiofrequency excitations²¹. These
90 ultrashort TE (UTE) pulse sequences have TEs about 10 to 20 times shorter than previously devel-
91 oped sequences and have been used to quantify both trabecular and cortical bone parameters²². Multi-
92 sequence MRI has been applied for the study of various musculoskeletal bones, joints and soft tissues
93²³. However, its potential for the estimation of trabecular parameters remains largely unclear and un-
94 explored.

95 In this work, we present a new technique for the prediction of trabecular parameters of bones in
96 children from multi-sequence MRI. Instead of performing the calculations directly on the MR images,
97 which is difficult due to the complexity and low-resolution of these images, we introduce a method
98 that learns statistically the relationship between the low-resolution MRI appearance in the cancellous
99 bone and the trabecular parameters as extracted from high-resolution image data. The estimation of
100 high-resolution information from low-resolution image data is a well-known problem in computer

101 vision^{24, 25}. In this work, a database of both MRI and HR-pQCT datasets of the same patients is col-
 102 lected and used as a training sample for a nonlinear regression model, which is subsequently used to
 103 predict the trabecular parameters conditioned on the information extracted from in vivo lower-
 104 resolution MR images. Due to the variation in the image properties and geometries of the trabecular
 105 areas, a collection of invariant image descriptors are calculated from the MRI images to obtain con-
 106 sistentlly the same level of information in all the cases. Feature selection is applied to select the de-
 107 scriptors that are the most relevant for the prediction of each trabecular parameter. The potential of the
 108 proposed technique is shown based on a data sample acquired from 96 children.



109

110 **FIG. 1.** Schematic diagram illustrating the main steps involved in the proposed statistical approach
 111 for the prediction of trabecular parameters conditioned on MR images.

112 II. METHODS

113 The aim of the proposed technique is to predict statistically the unknown trabecular indices based on
 114 the information contained within low-resolution MR images of the cancellous bone. By using a train-
 115 ing sample that contains both low-resolution and high-resolution data of the trabecular areas, we learn
 116 a predictive regression model by following the workflow schematically described in Figure 1 and the
 117 steps summarized as follows:

118 **Step 1:** Collect a data sample in which each individual undergoes both a multi-sequence MRI scan
 119 and a high-resolution HRpQCT scan of the same bone regions.

120 **Step 2:** Calculate the trabecular parameters using the high-resolution HRpQCT images.

121 **Step 3:** Delineate the trabecular bones on the MRI images.

122 **Step 4:** Calculate texture descriptors that describe the appearance patterns (variability, repeatability,
123 complexity) inside the trabecular region.

124 **Step 5:** Select for each sequence and trabecular parameter a subset of texture features with maximal
125 prediction power.

126 **Step 6:** Build a nonlinear regression model between the optimal textures and the trabecular parame-
127 ters, which is the output of the proposed method.

128 The details of these steps are now given in the subsequence Subsection II-A to II-C.

129 **A. Patient Data**

130 We recruited 96 volunteers aged 13 to 16 years old to undergo HRpQCT and skeletal MRI (sMRI) of
131 the non-dominant ultra-distal tibia at 1.5 T. Clinical pathologies were excluded from this study. The
132 non-dominant limb was scanned as this is standard practice in clinical studies due to the influence of
133 additional forces through physical activity for example. Participants were recruited from local adver-
134 tisements, from healthy cohorts who had taken part in previous bone-related research and from the
135 orthopedic clinic at Sheffield Children’s NHS Foundation Trust, UK. Written informed consent was
136 obtained from all participants. The following exclusion criteria were applied – known metabolic bone
137 disease, previous orthopedic surgery or fractures that preclude imaging at selected sites, history of
138 long term immobilization, known chronic/systemic illness, endocrine disorders, genetic syndromes,
139 use of oral or intravenous steroids, and known skeletal dysplasia, or any contraindications to MRI.

140 **HR-pQCT data acquisition:** HR-pQCT image acquisition and analysis of the distal tibia was per-
141 formed using the standard built-in software (XtremeCT, V 6.0, Scanco Medical AG, Brüttisellen,
142 Switzerland) and in accordance with the methods used previously by Paggiosi et al. ²⁶. In all post-
143 pubertal participants with fused tibial growth plates, a reference line was placed on the scan image at
144 the endplate of the distal tibia to indicate the position of the first measurement slice (22.5 mm and 9.5
145 mm proximal from the reference line for the tibia and radius respectively). In pre-pubertal and those

146 participants with open tibial and growth plates, the reference line was placed on the scan image at the
147 proximal end of the growth plate to indicate the position of the first measurement slice (1 mm proxi-
148 mal from the reference line)²⁶. All scans were performed using the non-dominant limb. A single stack
149 of parallel CT slices (110 slices = 9.02 mm) for each site was acquired in the high resolution mode
150 (image matrix = 1536 x 1536, in-plane resolution = 28 μm , acquisition time = 2.8 mins). Daily meas-
151 urements of the manufacturer device-specific phantom (Scanco Medical AG, Brüttisellen, Switzer-
152 land) were performed to monitor the stability of the XtremeCT. Tibial trabecular microstructural pa-
153 rameters measured were included trabecular number (Tb.N, 1/millimeters), trabecular thickness
154 (Tb.Th, millimeters), and trabecular separation (Tb.Sp, millimeters).

155 **MRI data acquisition:** All MRI data were acquired on a GE Signa Horizon HDXT 1.5 Tesla (Gen-
156 eral Electric, Milwaukee, WI, USA) whole body clinical system, using a manufacturer supplied ankle
157 coil. In this study, the MRI protocol included our standard routine T1-weighted Fast Spin Echo (T1),
158 T2-weighted Fast Spin Echo (T2), T2*-weighted Gradient Echo (T2*), Fast Imaging Employing
159 Steady State Acquisition (FIESTA) sequences used in clinical practice, along with Ultrashort Echo
160 Time Dual Echo (UTE) and Ultrashort Echo Time Dual Echo High-Resolution (UTE-HR) sequences
161 provided by the manufacturer for research purposes. The UTE sequences were acquired in three ver-
162 sions, i.e. UTE_1, UTE_2, and UTE_sub, which refer to the 1st and 2nd echoes of the dual echo se-
163 quence and their subtraction, respectively (similarly for the HR versions). We thus obtain a total of 10
164 MRI sequences in this study (T1, T2, T2*, FIESTA, UTE_1, UTE_2, UTE_sub, UTE_HR_1, UTE_
165 HR_2, UTE_HR_sub).

166 All imaging sequences were acquired in the axial plane and the pulse sequence parameters are pro-
167 vided in Table 1. Furthermore, the images were processed with the calibration process PURE (Phased
168 Array Uniformity Enhancement), which is a correction for non-uniform signal intensity from the re-
169 ceiver coil. Due to time constraints (i.e. keeping the scan time reasonably short), the subjects did not
170 have all sequences performed, but were randomly assigned a subset and the number of cases for each
171 sequence is given in Table 1. The slice thickness was tuned for each sequence in order to give a good
172 diagnostic quality image and without compromising signal to noise ratio, while the UTE high resolu-

173 **tion images generally have thinner slices.** Note that the same protocol used to define the region of
 174 interest (9.02 mm) for HRpQCT was also applied to skeletal MRI imaging to ensure that the same
 175 region of interest and the same limb was imaged for comparison.

176 **TABLE 1:** A summary of the MRI pulse sequence parameters used in the study.

Sequence	No. cases	TR (ms)	TE (ms)	α	Res. (mm)	FOV (mm)	No. slices	Slice Th. (mm)	Scanning time (mins)	Band-width (kHz)
T1	26	400	16.3	90°	0.35	180×180	12	3.0	2.20	20.83
T2	46	4000	98.2	90°	0.35	180×180	11	4.0	4.32	41.67
T2*	48	705	13.3	25°	0.35	180×180	11	4.0	5.22	13.89
FIESTA	27	5.93	2.67	80°	0.54	280×280	9	4.1	0.65	83.33
UTE	47	11.6	0.03/4.37	10°	0.5	140×140	20	3.0	4.18	62.5
UTE-HR	30	18.1	0.03/7.17	10°	0.3	140×140	10	2.0	6.21	62.5

177
 178 All the MR images were transferred in DICOM format onto a standard PC workstation and con-
 179 verted into the Analyze 7.5 (AnalyzeDirect Inc., Overland Park, KS, www.analyzedirect.com) file
 180 format using custom software. Regions of interest were then drawn to demarcate cortical bone, tra-
 181 becular bone and background noise on each sequence acquired in each patient, more specifically on
 182 the three slices proximal to the growth plate using 3Dslicer V 4.1.0 ²⁷ (Surgical Planning Lab,
 183 Brigham and Women’s Hospital, Boston, MA, www.slicer.org). These regions of interest were then
 184 exported in Analyze 7.5 format to provide tissue masks for further analysis, as illustrated schematical-
 185 ly in Figure 1.

186 **B. Textural Feature Descriptors**

187 The aim of this work is to build a predictive model of the form:

$$\mathbf{y}_{\text{Predicted}} = \mathbf{x}_{\text{MRI}} \mathbf{A}, \quad (1)$$

188 where \mathbf{A} is the regression matrix of the model, estimated statistically from the training sample as
 189 detailed below. In the proposed method, the output of the predictive model is simply a 3-dimensional
 190 vector that contains the three trabecular indices of interest, i.e.,

$$\mathbf{y}_{\text{Predicted}} = (y_1, y_2, y_3)^T, \text{ where } \begin{aligned} y_1 &= \text{Tb.Th}, \\ y_2 &= \text{Tb.Sp}, \\ y_3 &= \text{Tb.N}. \end{aligned} \quad (2)$$

191 For the input of the predictive model, we need a vector \mathbf{x}_{MRI} , which describes the appearance and
 192 the contextual information contained within of the cancellous bone in the MR images, as follows:

$$\mathbf{x}_{\text{MRI}} = (x_1, \dots, x_i, \dots, x_m)^T. \quad (3)$$

193 More specifically, we calculate m image texture descriptors from the entire cancellous bone area
 194 such that the computed properties are invariant to differences in bone shape and size, or to the number
 195 of slices used to image the bone. In other words, we choose feature descriptors that convey infor-
 196 mation about the trabecular appearance in the cancellous bone. From an image analysis perspective,
 197 trabeculae are patterns that can be characterized by the variability, repeatability, and/or complexity of
 198 the underlying image texture. In accordance with these notions, we can classify the features used here
 199 in these distinct types of of complementary nature as detailed below. The mathematical derivations of
 200 the descriptors are summarized in Table 2 to enable researchers to re-implement them.

201 **Statistical variability:** Moment-based statistical features are computed directly on image intensity
 202 values and will enable to obtain some information about the ratios of marrow and bone. The average
 203 intensity (feature 1 in Table 2) is expected to be higher or lower depending on greater relative quanti-
 204 ties of marrow and bone. The spread of the intensity values as captured in the standard and absolute
 205 deviations (features 2 and 3 in Table 2) may relate to the trabecular **regularity** more directly as indi-
 206 vidual voxel values are determined less or more by mixture of bone and marrow response. Other sta-
 207 tistical moment-based features we consider in this work are skewness (feature 4) and kurtosis (feature

208 5), which describe the shape of the distribution of the intensity values in the cancellous bone. Note
209 that for the statistical descriptors, the image intensity ranges were mapped linearly between 1 and 256
210 to obtain normalized intensities between subjects. While the limited intensity range of the cancellous
211 bone allowed this to be a sufficiently good approach, more sophisticated normalization approaches
212 should be considered to mitigate the risk of outlier intensities dominating the remapping, and to better
213 match the actually non-linear relationship between intensity values in different acquisitions.

214 **Repeatability of the patterns:** In this section we estimate Grey Level Co-occurrence Matrices
215 (GLCM's) ²⁸, which encode information about fixed-size neighborhoods and are parameterized by a
216 displacement vector d . The entry $G_{u,v}^d$ in a GLCM G^d reflects the frequency of observing the value u
217 at locations x in the ROI and value v at location $x + d$, also in the ROI. By using a fixed set of dis-
218 placements, we can build several GLCM's and combine them as appropriate for our application. In
219 this paper, we use the four in-plane displacements of 1 pixel (or actually $\sqrt{2}$ pixels for the two diago-
220 nal displacements) that comprise half of the 8-neighbourhood, as we are looking for features smaller
221 than our voxel sizes (trabeculae). Statistics on the summation of these four matrices are then used to
222 convey information about the regularity of patterns occurring (energy, entropy, maximum: features 6,
223 7, and 8, respectively), in addition to some information about the types of the patterns themselves
224 (contrast: feature 9; homogeneity: feature 10). Note that the maximum refers to the highest value in
225 the GLCM, or in other words the probability of the most likely co-occurring pair of intensities. This is
226 greatest when the maximum probability reaches its theoretical minimum (i.e. when the distribution is
227 uniform). For all the GLCM features, we estimated the 5th and 95th intensity percentiles for each
228 ROI, and the corresponding intensity range was mapped between 1 and 16 to ensure sufficient matrix
229 density.

230 **Complexity of the patterns:** In addition to measures like the GLCM entropy, we use run-length analy-
231 sis to establish a measure of complexity of the patterns. While the GLCM analysis is confined to fixed
232 neighborhood sizes, this analysis provides a complement in that it does not have such a limitation;
233 instead this encodes information for maximal areas (linear only) of equal or similar intensity in a run-
234 length matrix (RLM) R , where the entries $R_{u,v}$ indicate the relative frequencies of observing intensity

235 u a total of v consecutive times, under condition that such a sequence is immediately preceded and
 236 followed by either another intensity or the ROI boundary. From these summaries we obtain infor-
 237 mation about fragmentation (short primitive emphasis, long primitive emphasis: features 11 and 12 in
 238 Table 2), regularity (primitive length uniformity: feature 13) or lack of such variation (grey level uni-
 239 formity: feature 14). As with the GCLM, we compute this only in-plane, along image scan lines, and
 240 sum the RLM's obtained in the two directions. In this section, the image intensity ranges were
 241 mapped linearly between 1 and 32 to ensure sufficient matrix density. Note that stronger quantization
 242 would lead to greater numbers of long runs and likely a greater spread in run lengths, leading once
 243 more to sparse RLM's. Therefore, we used a quantization level different from that used to compute
 244 the GLCM's.

245 The final measures of complexity used are based on the Fractal Dimension (FD) of the image. The
 246 FD as proposed in ²⁹ measures, informally speaking, a ratio of the change in detail to the change in
 247 scale, by a log linear fit to the intensity standard deviations obtained at different rates of subsampling.
 248 While the run length features could work in only one dimension at a time, the FD works in two di-
 249 mensions. Using a differential box-counting approach ³⁰, the FD at each pixel in a slice is computed,
 250 resulting in the FD image F , and these are aggregated in the mean, standard deviation and lacunarity –
 251 the latter a measure of how densely the fractal fills the space it inhabits (features 15, 16, and 17 in
 252 Table 2). For more details on the method of computing the local FD , we refer to the appendix of ³¹.

253

254 **TABLE 2:** A summary of the image feature descriptors and their mathematical definitions, using
 255 image I , Region of Interest Ω (as a set of pixels/voxels), Grey Level Co-occurrence Matrix G , Run-
 256 length Matrix R , Fractal Dimension map F , and subscripts for indexing.”

Num.	Feature descriptor	Type	Equation
1	Mean	Statistical	$M(\Omega, I) = \frac{1}{\ \Omega\ } \sum_{i \in \Omega} I_i$

			$\mu_I = M(\Omega, I)$
2	Standard deviation	Statistical	$SD(\Omega, I) = \sqrt{\frac{\sum_{i \in \Omega} (I_i - \mu_I)^2}{\ \Omega\ }}$
3	Absolute deviation	Statistical	$AD(\Omega, I) = \frac{\sum_{i \in \Omega} I_i - \mu_I }{\ \Omega\ }$
4	Skewness	Statistical	$Sk(\Omega, I) = \frac{\frac{1}{\ \Omega\ } \sum_{i \in \Omega} (I_i - \mu_I)^3}{\left(\frac{1}{\ \Omega\ } \sum_{i \in \Omega} (I_i - \mu_I)^2\right)^{\frac{3}{2}}}$
5	Kurtosis	Statistical	$Kur(\Omega, I) = \frac{\frac{1}{\ \Omega\ } \sum_{i \in \Omega} (I_i - \mu_I)^4}{\left(\frac{1}{\ \Omega\ } \sum_{i \in \Omega} (I_i - \mu_I)^2\right)^2}$
6	Energy	Pattern/GLCM	$Ene(\mathbf{G}) = \sum_{i,j} G_{i,j}^2$
7	Entropy	Pattern/GLCM	$Ent(\mathbf{G}) = - \sum_{i,j} G_{i,j} \log G_{i,j}$
8	Maximum	Pattern/GLCM	$Max(\mathbf{G}) = \max_{i,j} G_{i,j}$
9	Contrast	Pattern/GLCM	$Contr(\mathbf{G}) = \sum_{i,j} i - j G_{i,j}$
10	Homogeneity	Pattern/GLCM	$Hom(\mathbf{G}) = \sum_{i,j} \frac{G_{i,j}}{1 + i - j }$
			$R_{tot} = R_{tot}(\mathbf{R}) = \sum_{a=1}^p \sum_{r=1}^{r_{max}} R_{a,r}$
11	Short primitive emphasis	Run-length	$SPE(\mathbf{R}) = \frac{1}{R_{tot}} \sum_{a=1}^p \sum_{r=1}^{r_{max}} \frac{R_{a,r}}{r^2}$

12	Long primitive emphasis	Run-length	$LPE(\mathbf{R}) = \frac{1}{R_{tot}} \sum_{a=1}^p \sum_{r=1}^{r_{max}} R_{a,r} \cdot r^2$
13	Primitive length uniformity	Run-length	$PLU(\mathbf{R}) = \frac{1}{R_{tot}} \sum_{r=1}^{r_{max}} \left(\sum_{a=1}^p R_{a,r} \right)^2$
14	Grey level uniformity	Run-length	$GLU(\mathbf{R}) = \frac{1}{R_{tot}} \sum_{a=1}^p \left(\sum_{r=1}^{r_{max}} R_{a,r} \right)^2$
15	Fractal dimension mean	Fractal dimension	$FDM(\Omega, F) = \frac{1}{\ \Omega\ } \sum_{i \in \Omega} F_i$
			$\mu_F = FDM(\Omega, F)$
16	Fractal dimension standard deviation	Fractal dimension	$FDSD(\Omega, F) = \sqrt{\frac{\sum_{i \in \Omega} (F_i - \mu_F)^2}{\ \Omega\ }}$
17	Fractal dimension lacunarity	Fractal dimension	$FDL(\Omega, F) = \frac{\frac{1}{\ \Omega\ } \sum_{i \in \Omega} F_i^2}{\left(\frac{1}{\ \Omega\ } \sum_{i \in \Omega} F_i \right)^2} - 1$

257

258 C. Nonlinear Regression Model

259 In this section we describe the technique used to build an optimal regression model that estimates the
260 missing trabecular parameters $\mathbf{y}_{\text{Predicted}}$ based on the values of the feature descriptors in the \mathbf{x}_{MRI} vector
261 (see Eq. (1)). More specifically, we need to define statistically the regression matrix \mathbf{A} such that the
262 predictions are optimal. Furthermore, we need to take into account the likely presence of non-linear
263 inter-dependencies in the data.

264 To achieve these goals, we implement a nonlinear regression model based on partial least squares
265 regression (PLSR)³², which has several suitable properties for the present work, in particular its abil-
266 ity to build optimal models from relatively small training samples, and its robustness to noise³².

267 Let us denote as $\mathbf{X} = (\mathbf{x}^{(1)}, \dots, \mathbf{x}^{(N)})$ the matrix of all the input data (we remove the index MRI from
 268 each \mathbf{x}_{MRI} for simplicity) as obtained from the N samples, and $\mathbf{Y} = (\mathbf{y}^{(1)}, \dots, \mathbf{y}^{(N)})$ the matrix of all
 269 the corresponding output trabecular parameters. The aim of PLSR is to perform a simultaneous de-
 270 composition of \mathbf{X} and \mathbf{Y} such that the score vectors obtained along the new representation axes of
 271 both the input and output matrices correlate best, thus leading to optimal predictions. One solution to
 272 the problem can be obtained through the NIPALS algorithm³³. More specifically, we wish to extract a
 273 set of t latent variables $\mathbf{C} = (\mathbf{c}_1, \dots, \mathbf{c}_t)$ from the input training data \mathbf{X} that correlate most with the
 274 output training trabecular vectors \mathbf{Y} . We perform a simultaneous decomposition of the input and
 275 output training data using the form:

$$\begin{aligned}\mathbf{X} &= \mathbf{C}\mathbf{P}^T \\ \mathbf{Y} &= \mathbf{D}\mathbf{Q}^T\end{aligned}\tag{4}$$

such that $\text{cov}[\mathbf{C}^T\mathbf{X}, \mathbf{D}^T\mathbf{Y}]$ is maximized.

276 Note that $\mathbf{D} = (\mathbf{d}_1, \dots, \mathbf{d}_t)$ are the latent trabecular variables after the decomposition (same thing for
 277 \mathbf{C} with respect to \mathbf{X}), while \mathbf{P} and \mathbf{Q} are the vector projections for the input \mathbf{X} and output \mathbf{Y} ma-
 278 trices, respectively.

279 The inherent nature of the extracted descriptors are likely to introduce a nonlinear interdependency
 280 between the input and output matrices \mathbf{X} and \mathbf{Y} . As a result, we use in this paper a kernel-based
 281 nonlinear implementation of PLSR as described in³⁴. The fundamental idea is to first perform a ker-
 282 nel transformation Φ of the input data, for example using a Gaussian kernel function. The kernel
 283 Gram matrix $\mathbf{K} = \Phi\Phi^T$ of the cross product between all input data points is obtained, which will act
 284 as the new input matrix to find the optimal predictors \mathbf{C} . Each element K_{kl} of the kernel matrix \mathbf{K}
 285 (of size N by N) is calculated as:

$$K_{kl} = K(x^{(k)}, x^{(l)}) = \exp(-\|x^{(k)} - x^{(l)}\|^2 / d),\tag{5}$$

286 where k and l are indices related to the N samples in the database. d is the width of the Gaussian
287 kernel and its value is obtained automatically through leave-one-out tests (i.e., by trying different
288 values and selecting the one that optimizes the trabecular predictions).

289 The decomposition of the matrices \mathbf{X} and \mathbf{Y} is then achieved using the iterative algorithm in Ta-
290 ble 3, which allows to obtain the matrices \mathbf{C} and \mathbf{D} . These are then used to obtain the final nonlinear
291 regression model:

$$\mathbf{y}_{\text{Predicted}} = \mathbf{K}(\mathbf{x}_{\text{MRI}})\mathbf{A}, \quad (6)$$

292 where \mathbf{A} is the optimal regression matrix calculated from the PLSR decomposition as:

$$\mathbf{A} = \mathbf{KD}(\mathbf{C}^T\mathbf{KD})^{-1}\mathbf{C}^T\mathbf{Y}. \quad (7)$$

293 Choosing a certain number of latent variables t in Table 3 enables to remove the information in the
294 input data that is less relevant to the predictions, and thus contributes to minimizing model over-
295 fitting. This number varies depending on the trabecular parameters (it is specific to each y_i
296 prediction) and it is defined the one that reduces prediction errors in leave-one-out tests.

297 Additionally, to further increase robustness to the size of the training sample, the final step of the
298 proposed technique is to apply a feature selection procedure³⁵ for each trabecular parameter and MRI
299 sequence, to select the best textural descriptors (i.e., those with the highest predictive power) to in-
300 clude in the vector \mathbf{x}_{MRI} and in the predictive model amongst the 17 variables described in Table 2.

301 More specifically, we start with the textural descriptor that gives the lowest prediction errors, and then
302 we iteratively add descriptors until the predictions stop improving. Generally, we found that between
303 three and six texture descriptors are sufficient to reach maximal prediction accuracy.

304

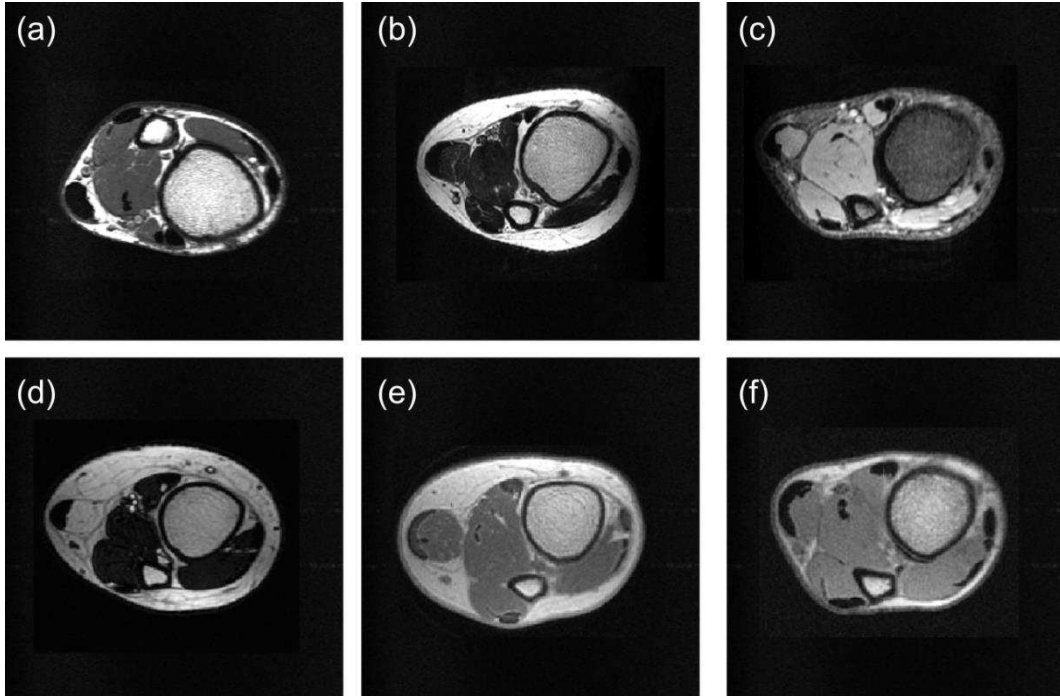
305

306

307

TABLE 3: Algorithm listing for the PLSR decomposition used in the regression model.

<p>Initialization: $\mathbf{K}_1 = \mathbf{K}$</p> <p>For each latent variable $k = 1 \dots t$</p> <p>(1) Initialize \mathbf{d}_k with one of the columns of \mathbf{Y}.</p> <p>(2) Calculate the input latent variable $\mathbf{c}_k = \mathbf{K}_k \mathbf{K}_k^T \mathbf{d}_k$, with $\ \mathbf{c}_k\ = 1$.</p> <p>(3) Update output scores $\mathbf{q}_k = \mathbf{Y}^T \mathbf{c}_k$;</p> <p>Calculate output latent vector $\mathbf{d}_k = \mathbf{Y} \mathbf{q}_k$, with $\ \mathbf{d}_k\ = 1$.</p> <p>(4) Repeat (2)-(3) until no change is noticed in \mathbf{c}_k</p> <p>(i.e. $\ \mathbf{c}_k - \mathbf{c}_{k-1}\$ is very small).</p> <p>(5) Remove the contribution of \mathbf{c}_k in \mathbf{K}_k for next iteration:</p> $\mathbf{K}_{k+1} = (\mathbf{I} - \mathbf{c}_k \mathbf{c}_k^T \mathbf{X}_k) \mathbf{X}_k (\mathbf{I} - \mathbf{c}_k \mathbf{c}_k^T \mathbf{X}_k).$ <p>End for</p>
--



309

310 **FIG. 2.** Examples of different subjects and different MRI sequences used in the experiments. (a) T1,
 311 (b) T2, (c) T2*, (d) FIESTA, (e) UTE_1, (f) UTE_2.

312 III. RESULTS

313 In this section, we evaluate the ability of the proposed statistical approach to estimate trabecular indi-
 314 ces (Tb.Th, Tb.Sp, and Tb.N) by using the selected MRI sequences considered in this study (see ex-
 315 amples in Figure 2) as the input of the prediction models. To this end, we run leave-one-out experi-
 316 ments such that the subject used for assessing the trabecular predictions is removed from the construc-
 317 tion of the feature-based regression models. For each test, we calculate the correlation coefficient
 318 (CC) as a measure of the extent of agreement between the values of the trabecular parameters $y_{\text{Predicted}}$
 319 as predicted from the low-resolution multi-sequence MR images by using the proposed statistical
 320 technique and the ground truth values of the parameters $y_{\text{HR-qQCT}}$ as estimated from the high-resolution
 321 HR-pQCT images.

322 **Prediction by using individual MRI sequences:** In the first experiment, we evaluate the prediction
 323 power of all MRI sequences separately for the prediction of all trabecular parameters. The obtained
 324 results are summarized in Table 4, where the sequences are listed in the descending order of the ob-

325 tained correlation coefficients. It can be seen that the MRI sequences have different levels of perfor-
326 mance. In general, the high-resolution UTE sequences UTE_HR_1 and UTE_HR_2 are those that
327 provide the best results (average CC = 0.63 and 0.61, respectively), followed by the two conventional
328 sequences FIESTA and T1 (average CC = 0.58 and 0.58, respectively). The calculation of p-values
329 shows that the differences between these sequences are not statistically significant ($p > 0.01$).
330 In general, the MRI sequences have an inconsistent performance as shown by the differences between
331 the maximal and minimal CC values across the trabecular indices (see last column of Table 4). For
332 example, with UTE_HR_2, there is a positive average CC of 0.70 in the prediction of Tb.N but this is
333 reduced to 0.53 for Tb.Sp. To obtain optimal predictions for all the parameters, one can use for exam-
334 ple three MRI sequences consisting of UTE_HR_1, UTE_HR_2, and FIESTA.

335 **TABLE 4:** Summary of the obtained correlation coefficients for the prediction of the parameters
336 Tb.Th, Tb.Sp, and Tb.N by using the different MRI sequences.

Sequence	Mean	Tb.Th	Tb.Sp	Tb.N	Max – Min
UTE_HR_1	0.63	0.55	0.71	0.61	0.16
UTE_HR_2	0.61	0.61	0.53	0.70	0.16
FIESTA	0.58	0.64	0.62	0.49	0.15
T1	0.58	0.60	0.68	0.47	0.21
UTE_HR_sub	0.57	0.41	0.63	0.67	0.25
UTE_2	0.53	0.50	0.61	0.49	0.11
T2*	0.47	0.54	0.48	0.41	0.12
T2	0.47	0.47	0.56	0.38	0.18
UTE1	0.46	0.50	0.44	0.45	0.06
UTE_sub	0.43	0.26	0.58	0.44	0.31

337

338

339 **Prediction by combining multiple MRI sequences:** In the last experiment, we investigate whether the
340 combination of multiple MRI sequences within a single predictive model can improve the predictions
341 for a given trabecular parameter. Thus we combine textural descriptors from different MRI sequences
342 into the input vector of the nonlinear regression model **by selecting those texture features that maxim-**
343 **ize prediction power following the method described in Section II-C.** The results of this experiment
344 are summarized in Table 5 for the three trabecular indices. It can be seen that that all the trabecular
345 parameters are slightly improved with this approach. For example, by combining T1 and FIESTA, the
346 Tb.Th is now estimated with a CC that reaches 0.68. Similarly, the estimation of Tb.Sp is achieved
347 this time with a CC = 0.75 by using UTE_HR_1 and UTE_HR_2, from a previous CC of 0.71 by
348 using UTE_HR_1 only. For Tb.N, however, the CC value decreases from 0.70 to 0.75 by using two
349 MRI sequences (T1 and UTE_SUB). **Generally, we found the improvement in performance by com-**
350 **binning multiple MRI sequences to be limited. This can be explained by the fact that combining multi-**
351 **ple sequences increases the dimensionality of the statistical model, which would therefore call for**
352 **additional datasets. Yet, in our case, the number of cases does not increase and even decreases for a**
353 **lot of the combinations. For example, T2 has 46 cases and UTE 47 cases, but these two sequences**
354 **have only 23 subjects in common in our sample. As a result, the combined models in the leave-one-**
355 **experiments become over-constrained and do not generalize well to new cases. Note that some com-**
356 **binations could not be tested because the MRI sequences did not have common subjects.**

357 **TABLE 5:** Prediction performance for each individual trabecular parameter
358 by combining multiple MRI sequences.

	Tb.Th	Tb.Sp	Tb.N
Correlation coefficients	0.68	0.75	0.73
Optimal combination of MRI sequences	T1 FIESTA	UTE_HR_1 UTE_HR_2	UTE_HR_1 UTE_HR_2
No. cases	26	30	30

359 IV. DISCUSSION

360 A. Current Performance

361 We presented in this paper a statistical approach to estimate trabecular parameters in children from
362 low-resolution MRI, without the need for acquiring high-resolution images of the bones that induce
363 significant radiation to a fragile population that is still under development and growth. The method
364 relates statistically the appearance of trabecular bones in low-resolution MR images with the trabecu-
365 lar parameters estimated from high-resolution images. The results show positive correlations between
366 the parameters predicted from the MRI sequences and those measured from HRp-QCT. In particular,
367 we found that the use of a single MRI sequence to drive the estimation of all the trabecular parameters
368 is not sufficient to obtain the most consistent results between all trabecular parameters. In comparison
369 correlation coefficients improved when individual sequences were used to predict single microstruc-
370 tural parameters, and were further optimized when dual combinations of sequences were used.

371 We found the high resolution UTE sequences UTE_HR_1 and UTE_HR_2 to have potential for the
372 prediction of trabecular parameters, with $CC > 0.70$ obtained for Tb.Sp and Tb.Th using these se-
373 quences. More research should be thus conducted to investigate these ultrashort TE pulse sequences
374 for the quantification of trabecular bone.

375 The proposed technique has two limitations that are worth mentioning. Firstly, due to its reliance
376 on low-resolution MRI, it is unlikely to provide the same performance for the analysis of the cortical
377 bone, which has currently a less well defined appearance in the MR images. Other research techniques
378 have been used to assess cortical bone but are not easily translatable into the clinical setting, or re-
379 quire sequences that are not currently available on clinical scanners ²⁰. Secondly, the application of
380 the technique to other populations such as for osteoporotic adults may not lead to the same perfor-
381 mance, as such patients vary significantly in the age range (from young to old adults) as well as in the
382 quality of the cancellous bone. Consequently, adaptation may be required such as by building multi-
383 class predictive models (depending on the disease class or age range). However, this study was specif-
384 ically designed to assess the feasibility of 1.5T MRI scanning for skeletal imaging in children, with a

385 view to significantly reduce their repetitive and harmful radiation exposure in longitudinal studies of
386 growth and development.

387 **B. Future Work**

388 In terms of clinical translation, the current results are very promising given the small size used to
389 build the models. However, one should aim for $CC > 0.9$ in order to obtain quantifications that can be
390 used in clinical practice. In this paper, we have demonstrated a first proof-of-concept of the potential
391 of low-resolution MRI to predict trabecular parameters, but there are several avenues that we are
392 planning to explore in order to enhance the accuracy of the technique and its clinical value.

393 **Training sample:** In this work, we have used models built with samples in the range of about 20 to
394 40 cases, which are unlikely to generalize well to more variable populations. While this has shown
395 promise, we plan to extend this work by collecting larger datasets (several hundred cases) from multi-
396 ple UK hospitals and with larger variability in the properties of the participants. This will lead to
397 models that are more robust and that have much higher coverage of bone variability.

398 **Prediction methodology:** We are also planning to improve the prediction framework in two main
399 directions. Firstly, in this preliminary study, we used a limited number of standard texture descriptors
400 (see Table 2) because the feature selection in the leave-one-out experiments is time consuming. How-
401 ever, we are planning in the future to implement a much more comprehensive list of texture de-
402 scriptors, including the most advanced and recent image representations developed by researchers in
403 the machine learning and image processing communities. Furthermore, we will investigate more ad-
404 vanced statistical prediction methods that can benefit from larger training samples, such as by em-
405 ploying decision trees^{36, 37}.

406 In summary, the proposed technique shows promise in the estimation of trabecular parameters in
407 children from low-resolution MRI by learning statistically the relationships between the statistical and
408 contextual information extracted from the cancellous bone in MRI and the parameters estimated in
409 HR-QCT. More generally, this statistical approach can promote the use of alternative modalities for in
410 vivo microstructural bone assessment in children and in various sites of the musculoskeletal system,
411 without the current limitations of high-resolution imaging modalities.

412 **REFERENCES**

- 413 1. Ruff C. Growth in bone strength, body size, and muscle size in a juvenile longitudinal sample. *Bone* 33: 317-
414 329, 2003.
- 415 2. Seeman E. and P. D. Delmas. Bone quality—the material and structural basis of bone strength and fragility.
416 *New England Journal of Medicine* 354: 2250-2261, 2006.
- 417 3. Williams B., D. Waddington, D. Murray and C. Farquharson. Bone strength during growth: influence of
418 growth rate on cortical porosity and mineralization. *Calcified tissue international* 74: 236-245, 2004.
- 419 4. Oliver H., K. A. Jameson, A. A. Sayer, C. Cooper and E. M. Dennison. Growth in early life predicts bone
420 strength in late adulthood: the Hertfordshire Cohort Study. *Bone* 41: 400-405, 2007.
- 421 5. Wren T. A. and V. Gilsanz. Assessing bone mass in children and adolescents. *Current osteoporosis reports* 4:
422 153-158, 2006.
- 423 6. Kirmani S., D. Christen, G. H. van Lenthe, P. R. Fischer, M. L. Bouxsein, L. K. McCready, L. J. Melton, B.
424 L. Riggs, S. Amin and R. Müller. Bone structure at the distal radius during adolescent growth. *Journal of Bone*
425 *and Mineral Research* 24: 1033-1042, 2009.
- 426 7. Bachrach L. K. Osteoporosis and measurement of bone mass in children and adolescents. *Endocrinology and*
427 *metabolism clinics of North America* 34: 521-535, 2005.
- 428 8. Dalle Carbonare L. and S. Giannini. Bone microarchitecture as an important determinant of bone strength.
429 *Journal of endocrinological investigation* 27: 99-105, 2004.
- 430 9. Brandi M. L. Microarchitecture, the key to bone quality. *Rheumatology* 48: iv3-iv8, 2009.
- 431 10. Genant H., P. Delmas, P. Chen, Y. Jiang, E. Eriksen, G. Dalsky, R. Marcus and J. San Martin. Severity of
432 vertebral fracture reflects deterioration of bone microarchitecture. *Osteoporosis international* 18: 69-76, 2007.
- 433 11. Chappard D., M.-F. Baslé, E. Legrand and M. Audran. Trabecular bone microarchitecture: A review.
434 *Morphologie* 92: 162-170, 2008.
- 435 12. Ulrich D., B. Van Rietbergen, A. Laib and P. Ruegsegger. The ability of three-dimensional structural
436 indices to reflect mechanical aspects of trabecular bone. *Bone* 25: 55-60, 1999.
- 437 13. Ding M., A. Odgaard and I. Hvid. Accuracy of cancellous bone volume fraction measured by micro-CT
438 scanning. *Journal of biomechanics* 32: 323-326, 1999.
- 439 14. Boutroy S., M. L. Bouxsein, F. Munoz and P. D. Delmas. In vivo assessment of trabecular bone
440 microarchitecture by high-resolution peripheral quantitative computed tomography. *The Journal of Clinical*
441 *Endocrinology & Metabolism* 90: 6508-6515, 2005.
- 442 15. Hulme P., S. Boyd and S. Ferguson. Regional variation in vertebral bone morphology and its contribution to
443 vertebral fracture strength. *Bone* 41: 946-957, 2007.
- 444 16. Sran M. M., S. K. Boyd, D. M. Cooper, K. M. Khan, R. F. Zernicke and T. R. Oxland. Regional trabecular
445 morphology assessed by micro-CT is correlated with failure of aged thoracic vertebrae under a posteroanterior
446 load and may determine the site of fracture. *Bone* 40: 751-757, 2007.
- 447 17. Burrows M., D. Liu and H. McKay. High-resolution peripheral QCT imaging of bone micro-structure in
448 adolescents. *Osteoporosis international* 21: 515-520, 2010.

- 449 18. Liu X. S., X. H. Zhang, K. K. Sekhon, M. F. Adams, D. J. McMahon, J. P. Bilezikian, E. Shane and X. E.
450 Guo. High-resolution peripheral quantitative computed tomography can assess microstructural and mechanical
451 properties of human distal tibial bone. *Journal of Bone and Mineral Research* 25: 746-756, 2010.
- 452 19. Krug R., J. Carballido-Gamio, S. Banerjee, A. J. Burghardt, T. M. Link and S. Majumdar. In vivo ultra-
453 high-field magnetic resonance imaging of trabecular bone microarchitecture at 7 T. *Journal of Magnetic
454 Resonance Imaging* 27: 854-859, 2008.
- 455 20. Wehrli F. W. Structural and functional assessment of trabecular and cortical bone by micro magnetic
456 resonance imaging. *Journal of Magnetic Resonance Imaging* 25: 390-409, 2007.
- 457 21. Robson M. D., P. D. Gatehouse, G. M. Bydder and S. Neubauer. Human imaging of phosphorus in cortical
458 and trabecular bone in vivo. *Magn Reson Med.* 51: 888-892., 2004.
- 459 22. Robson M. D., P. D. Gatehouse, M. Bydder and G. M. Bydder. Magnetic resonance: an introduction to
460 ultrashort TE (UTE) imaging. *J Comput Assist Tomogr.* 27: 825-846., 2003.
- 461 23. Berquist T. H. MRI of the musculoskeletal system. Lippincott Williams & Wilkins, 2012.
- 462 24. Freeman W. T., E. C. Pasztor and O. T. Carmichael. Learning low-level vision. *International Journal of
463 Computer Vision* 40: 25-47, 2000.
- 464 25. Zou W. W. and P. C. Yuen. Very low resolution face recognition problem. *IEEE Transactions on Image
465 Processing* 21: 327-340, 2012.
- 466 26. Paggiosi M. A., R. Eastell and J. S. Walsh. Precision of high-resolution peripheral quantitative computed
467 tomography measurement variables: influence of gender, examination site, and age. *Calcif Tissue Int.* 94: 191-
468 201. doi: 110.1007/s00223-00013-09798-00223. Epub 02013 Sep 00222., 2014.
- 469 27. Fedorov A., R. Beichel, J. Kalpathy-Cramer, J. Finet, J.-C. Fillion-Robin, S. Pujol, C. Bauer, D. Jennings,
470 F. Fennessy and M. Sonka. 3D Slicer as an image computing platform for the Quantitative Imaging Network.
471 *Magnetic resonance imaging* 30: 1323-1341, 2012.
- 472 28. Haralick R. M., K. Shanmugam and I. H. Dinstein. Textural features for image classification. *IEEE
473 Transactions on Systems, Man and Cybernetics* 610-621, 1973.
- 474 29. Mandelbrot B. B. The fractal geometry of nature. Macmillan, 1983.
- 475 30. Chen S. S., J. M. Keller and R. M. Crownover. On the calculation of fractal features from images. *IEEE
476 Transactions on Pattern Analysis and Machine Intelligence* 15: 1087-1090, 1993.
- 477 31. Al-Kadi O. S. and D. Watson. Texture analysis of aggressive and nonaggressive lung tumor CE CT images.
478 *IEEE Transactions on Biomedical Engineering* 55: 1822-1830, 2008.
- 479 32. Abdi H. Partial least squares regression (PLS-regression). Thousand Oaks, CA: Sage, 2003, p. 792-795.
- 480 33. Wold S., P. Geladi, K. Esbensen and J. Öhman. Multi-way principal components-and PLS-analysis. *Journal
481 of Chemometrics* 1: 41-56, 1987.
- 482 34. Rosipal R. and L. J. Trejo. Kernel partial least squares regression in reproducing kernel Hilbert space. *The
483 Journal of Machine Learning Research* 2: 97-123, 2002.
- 484 35. Guyon I. and A. Elisseeff. An introduction to variable and feature selection. *The Journal of Machine
485 Learning Research* 3: 1157-1182, 2003.

- 486 36. Dietterich T. G. An experimental comparison of three methods for constructing ensembles of decision trees:
487 Bagging, boosting, and randomization. *Machine learning* 40: 139-157, 2000.
- 488 37. Prasad A. M., L. R. Iverson and A. Liaw. Newer classification and regression tree techniques: bagging and
489 random forests for ecological prediction. *Ecosystems* 9: 181-199, 2006.